THE JOURNAL OF PHYSICAL CHEMISTRY C
A JOURNAL OF THE AMERICAN CHEMICAL SOCIETY

pubs.acs.org/JPCC

Article

Compositional Fluctuations Mediated by Excess Tellurium in Bismuth Antimony Telluride Nanocomposites Yield High Thermoelectric Performance

Nagendra S. Chauhan,* Sergey V. Pyrlin, Oleg I. Lebedev, Luis S. A. Marques, Marta M. D. Ramos, Tanmoy Maiti, Kirill Kovnir, Brian A. Korgel, and Yury V. Kolen'ko*

Cite This: J. Phys. Chem. C 2021, 125, 20184–20194

Read Online

ACCESS | Metrics & More | Article Recommendations | Supporting Information

ABSTRACT: A high thermoelectric figure of merit (ZT) in state-of-the-art bismuth antimony telluride (BST) composites was attained by an excess tellurium-assisted liquid-phase compaction approach. Herein, we report a maximum ZT of ≈ 1.4 at 500 K attained for BST bulk nanocomposites fabricated by spark plasma sintering of colloidally synthesized $(Bi,Sb)_2Te_3$ platelets and Te-rich rods. The Te-rich nanodomains and antimony precipitation during sintering result in compositional fluctuations and atomic ordering within the BST−Te eutectic microstructure, which provides additional phonon scattering and hole contributions. The electrical transport measurement and theoretical calculations corroborate the altered free carrier density *via* lattice defects and atomic ordering under Te-rich conditions, resulting in a higher power factor. Microstructural studies suggest that reduction in lattice thermal conductivity is due to composite interfaces and defects in the closely packed $(Bi,Sb)_2Te_3$ matrix with unevenly distributed Sb- and Te-rich nanodomains. This work provides an unconventional chemical synthesis route with large scalability for developing high-performance chalcogenide-based bulk nanocomposites for thermoelectric applications.

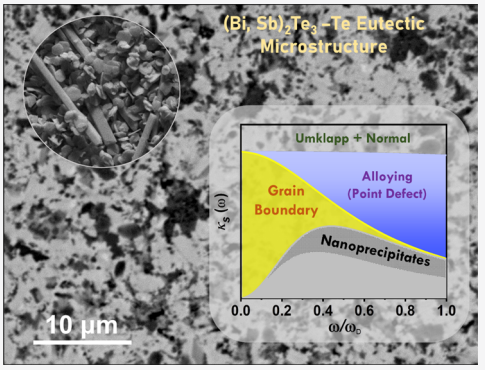

1. INTRODUCTION

Solid-state thermoelectric (TE) transport phenomena involve direct interconversion between heat and electricity, which are actively studied nowadays for applications involving waste heat recovery, remote power supplies, portable device cooling, and so forth.[1−4] Such TE-based energy conversion devices operate either in the power generation mode due to the Seebeck effect or in the refrigeration mode *via* the Peltier effect. However, in both of these modes, efficiency of energy conversion is determined using the same dimensionless TE figure of merit (ZT), which is conventionally expressed as $ZT = (S^2\sigma/\kappa)T$, where S, σ, and κ represent the Seebeck coefficient, electrical conductivity, and thermal conductivity at the absolute temperature (T), respectively.[5,6] To maximize the TE energy conversion efficiency, higher ZT and larger temperature differential (ΔT) between the hot and cold sides are needed. However, owing to intrinsic difficulties in decoupling electrons and phonons in bulk solids for ZT enhancement, the TE conversion efficiency of bulk materials continues to remain low, when compared with the other existing waste heat recovery technologies, such as organic rankine cycles, recuperators, regenerators.[7]

Nevertheless, TE offers a promising prospect for power generation from heat with ZT > 1 materials in the near-room temperature regime, wherein bismuth antimony telluride (BST) and its derivatives have remained the state-of-the-art TE material and have been extensively used for cooling applications in most successfully commercialized Peltier refrigerators.[6,8] It is widely recognized that $(Bi,Sb)_2Te_3$ solid solutions exhibit the highest ZT among any of the existing materials in the near-room temperature regime due to their relatively high carrier mobility, μ, and lower lattice thermal conductivity, κ_L. Despite the possibility of alloying the Bi_2Te_3−Sb_2Te_3 system as p-type or n-type materials, these alloys are widely recognized as excellent p-type materials with $Bi_{0.5}Sb_{1.5}Te_3$ as the most optimized composition.[8] To further enhance the ZT of this optimally alloyed composition, doping with Cu,[9,10] Cd,[11] Ag,[12,13] and Pb[14] and nanostructuring *via* ball milling,[9,10,13,15,16] melt spinning,[17−19] and chemical synthesis[20,21] have been extensively carried out. Similarly, composite aspects of hybridization with nanoparticles (NPs) such as Bi,[22] Sb_2O_3,[23] SiC,[24] ZnO,[25] Zn_4Sb_3,[26] PbSe,[27] Y_2O_3,[28]

Received: June 18, 2021
Published: September 13, 2021

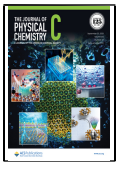

https://doi.org/10.1021/acs.jpcc.1c05375
J. Phys. Chem. C 2021, 125, 20184−20194

and SiO_2[29] were demonstrated for tuning the TE transport favorably.

Lately, unconventional nanocomposite approaches with a Te-excess composition[18,20,30−32] have been found to be most effective in attaining higher ZT. For instance, an ultralow κ of $\approx$ 0.33 W m^{-1} K^{-1} due to dense dislocation arrays embedded in grain boundaries by liquid-phase compaction of 25 wt % excess Te in $Bi_{0.5}Sb_{1.5}Te_3$ bulks resulted in a ZT of $\approx$ 1.86 at 320 K.[18] Similarly, formation of crystallographically textured nanomaterials by a solution re-precipitation mechanism led to an unprecedented ZT of $\approx$ 1.96 at 420 K.[20] It is noteworthy that these high-performance Te-excess compositions were optimized by adjusting the nominal Te−(Bi + Sb) ratio to $\approx$1.7,[18,20,30,32] that is, at $\approx$10 at. % Te excess, rather than the stoichiometric Te−(Bi + Sb) ratio $\approx$1.5. Excess Te ($\sim$10 at. %) in $(Bi,Sb)_2Te_3$ alloys results in precipitation of the Te-rich phase, which substantially reduces the lattice thermal conductivity without deteriorating the power factor (PF) ($S^2\sigma$), thus resulting in higher ZT.[18,20,30,32] Additionally, in nearly stoichiometric compositions with small excess Te (*i.e.*, less than 5 at. % Te), the hole concentration decreases with increasing Te content, which is mainly attributed to suppression of the antisite defects (Bi_{Te} and Sb_{Te}) and Te vacancies.[11,20] Thus, excess Te in $(Bi,Sb)Te_{3+x}$ nanocomposites plays a significant role in determining the electrical transport properties and reducing the thermal conductivity, which can be effectively employed for attaining optimal phonon and electron transport properties within and beyond the alloy limit.

Alongside phase constitution, synthesis methodology and processing temperature play a vital role in determining the physical and transport properties, particularly in $(Bi,Sb)_2Te_3$ alloys, which is largely due to their propensity toward nonstoichiometry and tellurium volatility.[33] To further enhance the ZT in p-type $Bi_{2-x}Sb_xTe_3$-based materials, which are commercially synthesized using zone melting methods, nanostructuring using ball milling followed by bulk consolidation employing hot pressing has been most successfully demonstrated.[17,20,34] However, severe plastic deformation during the milling process was found to induce a "donor-like" effect, which promotes minority charge carriers, that is, electrons, thereby deteriorating the electrical properties.[33,35] Alternatively, chemical synthesis[36−38] provides a convenient means of obtaining nanocrystals, while spark plasma sintering (SPS)[30,33,39,40] offers higher heating rates to prevent grain growth and achieve higher densification.

Recently, we established an alternative colloidal synthesis route for obtaining complex metal chalcogenide NPs.[41−43] In this work, we broaden the scope of our scalable colloidal synthesis to attain colloidal Bi−Sb−Te nanoplatelets and Te-rich nanorods. These NPs were subsequently consolidated employing SPS into bulk nanocomposites exhibiting a maximum ZT of $\approx$ 1.4 at a higher temperature of 500 K as compared to the state-of-the-art BST alloys. The microstructural changes during sintering were found to be accompanied by telluride spilling and antimony *in situ* precipitation as secondary phases, which resulted in compositional fluctuations and atomic ordering within the Bi−Sb−Te matrix, thereby providing additional phonon scattering with a minimal effect on carrier scattering and mobility. The detailed structural characterization and transport property measurement were correlated, and TE performance of the bulk nanocomposites was understood using theoretical inputs for low-temperature TE-based power generation applications.

2. EXPERIMENTAL DETAILS

2.1. Reagents. Bismuth(III) acetate [$Bi(ac)_3$, 99.99%, Sigma-Aldrich], antimony(III) acetate [$Sb(ac)_3$, 99.99%, Sigma-Aldrich], diphenyl ditelluride (Ph_2Te_2, 97%, Acros Organics), and hexadecylamine (HDA, 95.0%, TCI) were used without further purification. The analytical reagent-grade absolute ethanol and toluene were obtained from Fisher Scientific.

2.2. Synthesis of Bi−Sb−Te Nanocrystals. The synthesis of $(Bi,Sb)_2Te_3$ NPs was performed in a three-neck round-bottom flask under an inert atmosphere employing the standard Schlenk line techniques. For a typical experiment, HDA (60 g, 248.5 mmol), $Bi(ac)_3$ (1.44 g, 3.73 mmol), $Sb(ac)_3$ (3.35 g, 11.2 mmol), and Ph_2Te_2 (4.98 g, 12.3 mmol) were loaded under air into a 250 mL three-neck round-bottom flask equipped with a magnetic stirring bar, vacuum adapter, thermocouple, and condenser. The flask was connected to the Schlenk line, and the mixture was heated to 383 K with continuous stirring to melt the solid HDA and allow homogenization of reagents. At 383 K, degassing for 3 h was done for the removal of low-boiling point liquids, such as possible water and acetic acid admixtures from the mixture.

Subsequently, the mixture was rapidly heated to 573 K and kept at 573 K for 1 h under Ar with continuous stirring, to assist desirable end-product formation within the solution. Thereafter, the resultant reaction mixture was cooled to 343 K and diluted with 100 mL of toluene under continuous stirring. After cooling to room temperature, the NPs were precipitated by the addition of a solvent mixture comprising toluene and ethanol (3:1) and collected by centrifugation at 9000 rpm for 5 min. The resultant solid precipitate, as displayed in Figure S1a, was washed twice with the same solvent mixture and centrifugation conditions. Thereafter, the solid end product shown in Figure S1b was dried in vacuum and homogenized using an agate mortar and pestle. Subsequently, the obtained fine powder was examined using elemental analysis, X-ray diffraction (XRD), and electron microscopy for effective removal of organic ligands and residues attached around the NPs.

2.3. Structural Characterization. Powder XRD patterns were collected using an X'Pert PRO diffractometer (PANalytical) equipped with Cu K_α radiation and a PIXcel detector. The XRD patterns were matched to the International Centre for Diffraction Data (ICDD) PDF-4 database using the HighScore software package (PANalytical), and Rietveld refinement was carried out using the FullProf Suite Rietveld program.[44] The phase mapping and morphological features were studied by scanning electron microscopy (SEM) using a Helios NanoLab 450S DualBeam microscope (FEI) and Tungsten-Electron Microscope (W-SEM, *Model: JSM-6010LA; JEOL*). High-angle annular dark-field scanning transmission electron microscopy (HAADF-STEM), selected area electron diffraction (SAED), and energy-dispersive X-ray spectroscopy in the STEM mode (STEM-EDX) studies were performed using a JEM-ARM200F cold FEG probe and image aberration-corrected microscope, operated at 200 kV, and equipped with a large-angle CENTURIO EDX detector.

2.4. Bulk Consolidation. The resultant Bi−Sb−Te nanopowder was subsequently consolidated into a BST bulk nanocomposite by sintering at rapid heating rates employing

https://doi.org/10.1021/acs.jpcc.1c05375
J. Phys. Chem. C 2021, 125, 20184−20194

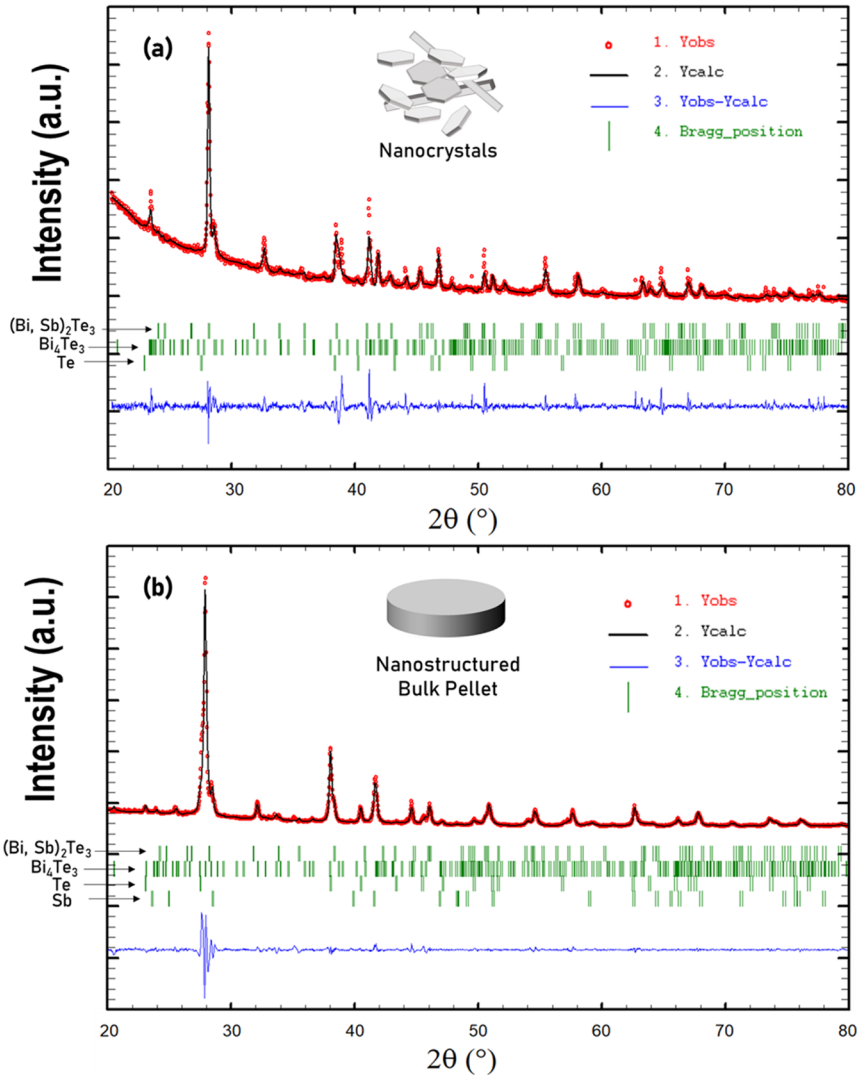

Figure 1. Rietveld refinement of experimental powder XRD patterns for the colloidally synthesized Bi−Sb−Te NPs (a) and BST bulk nanocomposite prepared by the SPS consolidation of the Bi−Sb−Te NPs (b).

SPS. The synthesized NPs were loaded into a graphite die of 12.7 mm diameter and sintered at 700 K with a pressure of ≈50 MPa under a vacuum of ≈4−6 Pa for the compaction of the nanopowder into denser pellets (hereafter referred to as BST). The density of the SPS-sintered bulk Bi−Sb−Te nanocomposites obtained as pellets with dimensions Ø 12.7 mm × 2 mm was measured using the Archimedes principle (822 e Mettler Toledo) and found to be ≈6.5 ± 0.2 g cm^{-3}.

2.5. TE Characterization. The TE transport measurements were performed in directions both parallel (cross-plane) and perpendicular (in-plane) to the pressing direction, as indicated in Figure S2. For thermal diffusivity (D) measurement, a circular disk specimen (Figure S2b) of ≈12.7 mm diameter and ≈2.2 mm thickness was used with a laser flash analyzer (M/s Linseis, LFA-1000). The total thermal conductivity was calculated using the expression $D \times C_p \times d$, where d is the density and C_p is the specific heat. The thermal diffusivity measurement was carried out only along the cross-plane direction due to the disk-shaped sample requirement. The electrical conductivity and Seebeck coefficient measurements were conducted using a four-probe DC method (ULVAC, ZEM-3) in a helium atmosphere on the sample cut into rectangular bars with approximate dimensions of 10 mm × 2 mm × 2 mm (Figure S2c) along both in-plane and cross-plane directions. The accuracies in the transport measurement are ±6% for thermal diffusivity, ±7% for electrical conductivity, ±7% for the Seebeck coefficient, ±10% for specific heat, and ±1% for density. The details of *ab initio* calculations of the electronic properties and Debye−Callaway model-based simulation for estimating the lattice thermal conductivity of the bulk $(Bi,Sb)Te_3$ nanocomposite are provided in Sections S3 and S4, respectively, of the Supporting Information.

3. RESULTS

3.1. NP Synthesis and Fabrication of the Bulk BST Nanocomposite. The selected composition was determined based on high ZT attained in optimal $Bi_{0.5}Sb_{1.5}Te_3$,[8,15,18] while the synthesis procedure and reaction conditions were guided by our recently developed colloidal synthesis route for chemical synthesis of complex metal chalcogenide NPs.[42] An excess 10 mol % Ph_2Te_2 was used for the reaction with $Bi(ac)_3$ and $Sb(ac)_3$ in HDA to account for the volatile nature and high vapor pressure of Te[20] and keeping in mind the high ZT

https://doi.org/10.1021/acs.jpcc.1c05375
J. Phys. Chem. C 2021, 125, 20184−20194

attained in Te-excess compositions that is 10 at. % excess Te in $Bi_{0.5}Sb_{1.5}Te_3$.[18,20,30,32] The Rietveld refinement of the XRD pattern of the synthesized end product is shown in Figure 1a, which corresponds to a mixture of phases identified as $BiSbTe_3$, Bi_4Te_3, and Te. The refined parameters of these structurally similar phases are presented in Table S1. The HDA-based chemical synthesis route was initially employed to synthesize NPs on the gram scale and was subsequently scaled up. The yield of the as-synthesized mixed-phase Bi−Sb−Te NPs for each batch was estimated to be *ca.* 90% (≈4.5 g) from the presented colloidal chemistry approach.

The Rietveld-refined XRD patterns of the sintered BST pellets, as shown in Figure 1b, are well indexed with the corresponding phases observed in the NP building blocks with some additional peaks corresponding to Sb. After SPS, the appearance of Sb peaks is in compliance with the previous observation of current-induced grain boundary modification and Sb nanoprecipitation in electrically sintered BST due to passage of high-density pulsed current ($\approx 10^3$ A cm^{-2}).[45] The sintering profile for bulk BST nanocomposite synthesis (Figure 2) comprises three steps, wherein temperature and pressure are raised simultaneously. The average ramp rate for heating and cooling was *ca.* 40 and 100 K min^{-1}, respectively. The maximum temperature of ≈700 K at which samples were sintered is close to the melting point of the Te-rich eutectic, suggesting the possibility of Te spilling due to liquid-phase sintering. However, the absence of isothermal sintering at the maximum temperature prevents the extent of Te spilling considerably, with lesser sample-to-sample variation for better processing and stoichiometric control.

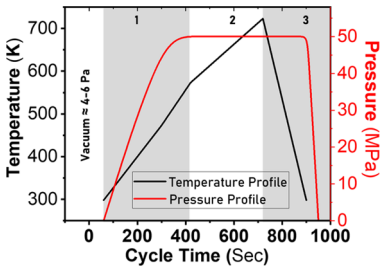

Figure 2. SPS profile.

3.2. Microstructural Characterization Reveals a Eutectic Microstructure with Antisite Defects. Detailed microstructure studies by SEM and TEM imaging on the mixed-phase Bi−Sb−Te NPs are shown in Figure 3. The SEM image (Figure 3a) revealed homogeneous sub-micron size distribution of Bi−Sb−Te particles with nanoplates having a thickness range of about a few tens of nanometers. Also, particles with a nanorod morphology having broad size distribution were simultaneously present along with nanoplatelets throughout the sample. The HAADF-STEM observation at low magnification of the nanosized feature with the plate (Figure 3b) and rod (Figure 3c) morphology and the respective STEM-EDX mappings revealed homogeneous distribution of the Bi, Sb, and Te elements in these particle appearances. Remarkably, particles with nanorod morphology display a Te-rich chemical composition, as confirmed by EDX analysis. To elucidate the structural arrangement in Bi−Sb−Te particles synthesized by colloidal synthesis, we further conducted HAADF-STEM study in conjunction with SAED analysis (Figure 3d). The representative high-resolution HAADF-STEM images of the as-synthesized plate-like particle along [100] zone axes, together with the respective SAED patterns displayed in Figure 3e, indicate a highly crystalline and remarkably defect-free sample.

The microstructural characterization of the representative SPS-sintered bulk BST nanocomposite sample is shown in Figure 4, which reveals a eutectic type of microstructure. At lower magnification, a well-distributed darker region within a brighter appearing matrix was evidenced in both secondary electron (SE) and backscattered electron (BSE) images, shown in Figure 4a,b, respectively. The EDX analysis of the matrix

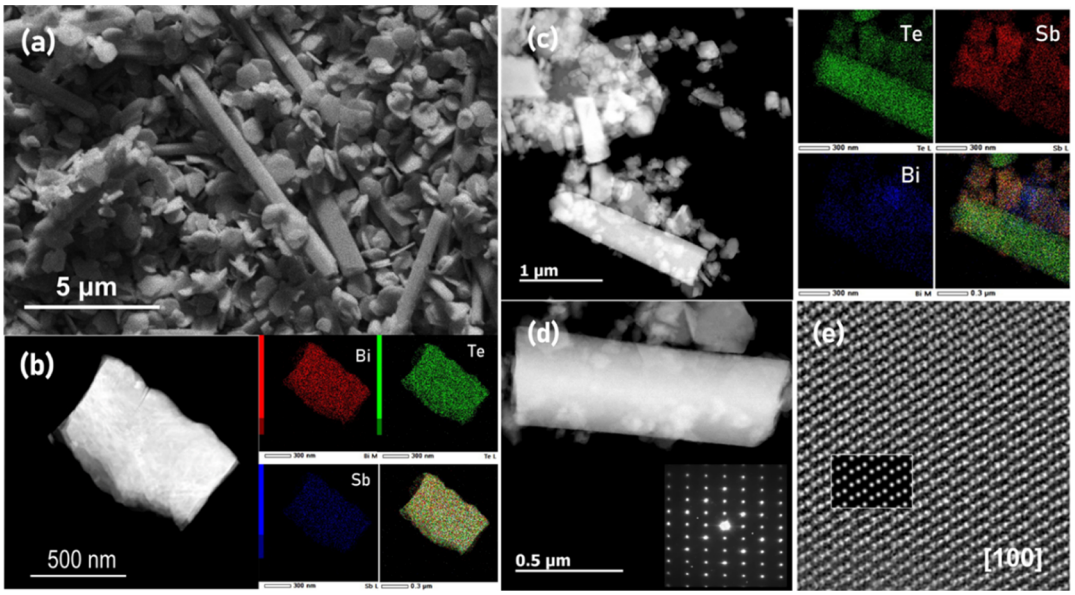

Figure 3. Microstructural characterization of Bi−Sb−Te NPs: (a) SEM image and HAADF-STEM image of the NPs with (b) plate morphology and (c) rod-shaped morphology along with the corresponding EDX elemental mapping of Bi, Sb, and Te and an overlaid color image. (d) HAADF-STEM image of a Te nanorod shown at higher magnification along with its corresponding SAED pattern shown in the inset, together with the respective high-resolution image along the [100] zone axis (e).

https://doi.org/10.1021/acs.jpcc.1c05375
J. Phys. Chem. C 2021, 125, 20184−20194

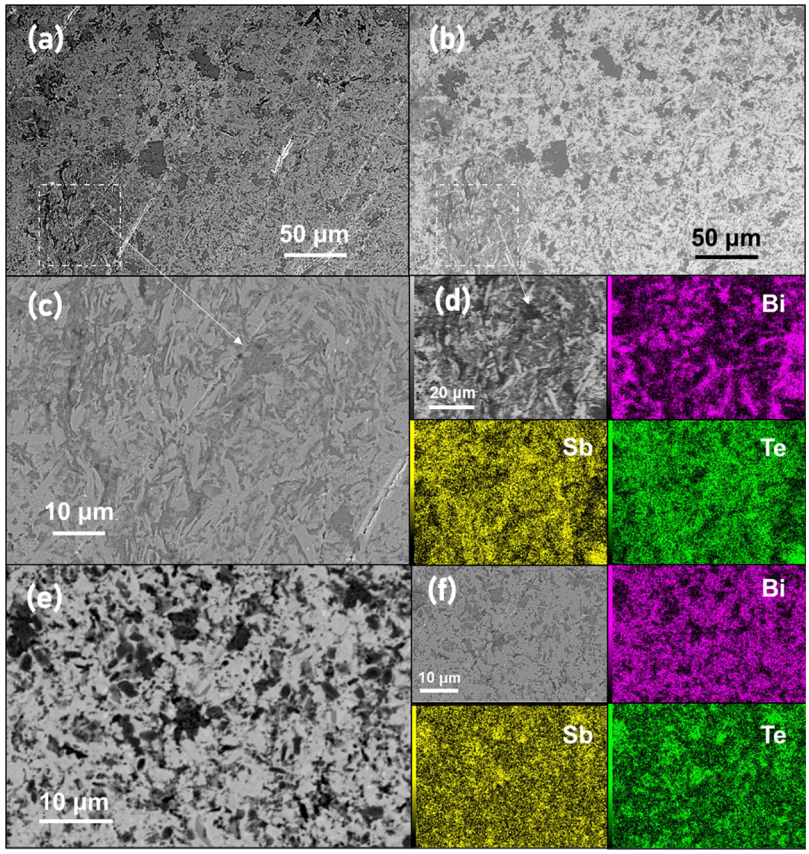

Figure 4. Microstructural characterization of the Bi−Sb−Te nanocomposite. Well-distributed darker regions at lower magnification within the brighter matrix displayed by (a) SE and (b) BSE images. The presence of dense dislocations in darker regions is probed at a higher magnification using (c) SE along with the corresponding (d) BSE images and elemental mapping. The secondary phases within the BST matrix, shown at higher magnification by (e) SE and (f) BSE images along with elemental mapping, are Te-rich and assigned to Te nanorods. The Te-rich phase serves as an active matrix, which promotes *in-situ* Sb precipitation, as revealed by dark and gray regions corresponding to *in-situ* Sb nanoprecipitates and Te-rich regions, respectively, in the BST−Te eutectic microstructure.

indicates varying at. % of $Bi_xSb_{2-x}Te_3$, where x varies throughout the matrix, having an average chemical composition of $BiSbTe_3$ indicated for the brighter regions. Dense dislocations marked by squares were observed sparsely, indicating liquid compaction.[18] At higher magnification in SE (Figure 4c) and BSE (Figure 4d) images, these dislocations show a random and diffused alignment. The elemental mapping indicates compositional fluctuations, wherein darker arrays were found to be rich in Te and Sb. This can be explained by liquid-phase sintering considering that Te-rich rods, as the wetting liquid, penetrate into the grain boundaries of the bright-appearing $(Bi,Sb)_2Te_3$ matrix, thus allowing atomic disorder owing to higher diffusivities and diffusion lengths of dislocations at the grain boundaries.[18]

Despite Te vaporization being prevalent at a higher sintering temperature of ≈700 K, a eutectic type of microstructure with decreased interface density was observed. Although a liquified excess Te phase remains nearly insoluble in the $(Bi,Sb)Te_3$ matrix,[18,46] it was found to induce compositional variations, which was probed at higher magnification. Evidently from the BSE image (Figure 4e), a dark region was found to develop over gray domains within the bright-appearing matrix. While gray regions correspond to Te nanodomains corresponding to Te nanorods (Figure 3c), dark regions are sites where antimony precipitation was found to be prevalent. The elemental mapping indicates an overlap of Sb-rich and Te-rich regions, which suggests that antimony precipitation is more likely to occur in Te-rich nanodomains.

The observed microstructural change and atomic ordering in the SPS-sintered BST sample suggest current-induced electromigration of constituent elements due to thermal activation during sintering in the bulk nanocomposite.[45] The presence of well-distributed Te and Sb precipitates within the BST matrix having a varied atomic ratio of Bi−Sb is favorable for enhancing phonon scattering. The uniformly distributed secondary phases within the SPS-consolidated BST matrix and their implication on the electrical and thermal transport properties of the BST nanocomposite are further analyzed by theoretical predictions and transport property measurements.

3.3. BST with High PF and Low Thermal Conductivity.

The Bi−Sb−Te-based compounds belong to a class of layered semiconductors with anisotropic TE properties, due to its anisotropic transport properties, which originate from the intrinsically misfit layered crystal structures.[47,48] The electrical transport properties, that is, σ and S, were experimentally measured along both in-plane and cross-plane directions. For theoretical comparison and understanding, the TE coefficients were estimated along the axis of the hexagonal unit cell (c-axis) and perpendicular to it (along the ab plane). This is also because in the case of $(Bi,Sb)_2Te_3$-based materials, the directions of the high charge mobility also correspond to the plane of easy cleavage of the crystal. Therefore, the c-axis of the $(Bi,Sb)_2Te_3$ lattice is mostly oriented along the short side of

https://doi.org/10.1021/acs.jpcc.1c05375
J. Phys. Chem. C 2021, 125, 20184−20194

the plate-like NPs, which in turn is most likely oriented along the cross-plane direction of the nanocomposite BST sample. The electrical transport parameters σ and S are shown in Figure 5a,b, which indicate p-type electrical conductivity with

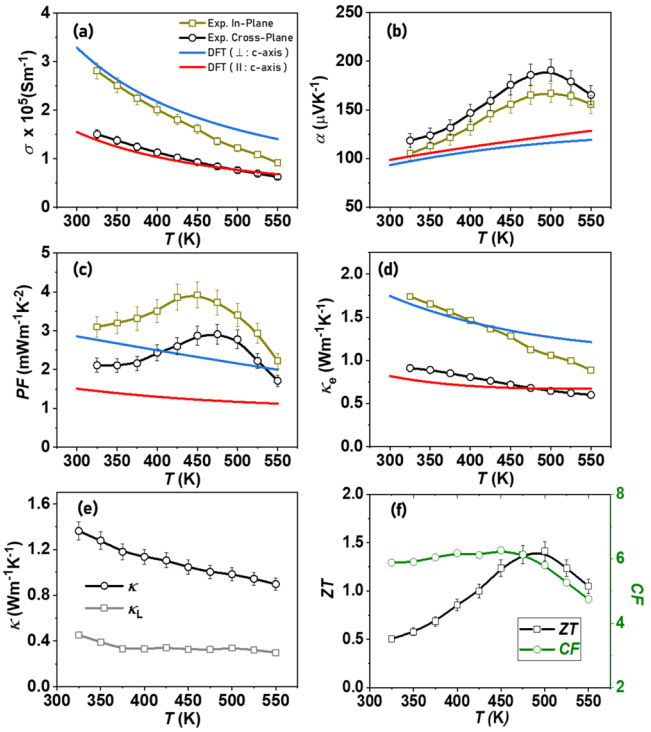

Figure 5. Temperature-dependent transport properties of the synthesized Bi−Sb−Te bulk nanocomposite, BST, (a) electrical conductivity, (b) Seebeck coefficient, (c) PF, (d) electronic thermal conductivity, (e) total and lattice thermal conductivity, and (f) TE figure of merit (ZT) and TE compatibility factor (CF).

degenerate semiconducting behavior in the measured temperature regime. A higher value of σ was observed along both in-plane ($\sigma_{\text{in-plane}}$) and cross-plane ($\sigma_{\text{cross-plane}}$) directions, which is comparable to previously reported σ for BST compounds.[17,20,48,49] The $\sigma_{\text{in-plane}}$ was found to be significantly higher than $\sigma_{\text{cross-plane}}$, as estimated theoretically, in line with previous experimental observation,[20] which can be ascribed to crystallographic anisotropy in BST-based compounds.

To further understand the electrical transport, room temperature hall measurement was carried out along the cross-plane direction. The carrier mobility μ of $\approx 115 \pm 5$ cm^2 V^{-1} s^{-1} and carrier concentration $n \approx 8.2 \pm 0.5 \times 10^{19}$ cm^{-3} were measured for the representative specimens, suggesting a higher n and lower μ for the synthesized BST nanocomposite, when compared with a previous report[50] on the BST nanograined bulk material ($n \approx 2.5 \times 10^{19}$ cm^{-3}; $\mu \approx 264$ cm^2 V^{-1} s^{-1}) and BST bulk ingot ($n \approx 1.8 \times 10^{19}$ cm^{-3}; $\mu \approx 298$ cm^2 V^{-1} s^{-1}). The higher carrier concentrations can be ascribed to defect chemistry in the synthesized BST primarily due to Sb vacancies in the BST matrix formed due to Sb nanoprecipitation at Te-rich eutectic domains (Figure 4). In the synthesized isoelectronic alloyed BST under Te-rich conditions, by taking into consideration the higher proportion of Sb_2Te_3 over Bi_2Te_3 and a comparatively lower formation energy of electron acceptor (Sb_{Te}) antisite defects over electron donor (Te_{Sb} and Te_{Bi}) defects, BST remains p-type despite Te-rich conditions mainly due to intrinsic hole doping. The presence of Sb vacancy defects within the BST matrix tends to enhance the n remarkably, resulting in a higher σ and correspondingly a lower Seebeck coefficient at near room temperature in comparison to a previous report on p-type BST alloys.[15,18,20,49]

The measured thermopower (Seebeck coefficient, S) is substantially higher than theoretical estimates and exhibits relatively lesser influence than its counterpart σ for anisotropy. The suppressed bipolar conduction and shifting of thermal excitation of minority charge carriers to higher temperature were observed for S along both in-plane ($S_{\text{in-plane}}$) and cross-plane ($S_{\text{cross-plane}}$) directions, with a maximum value of around 500 K. As observed, $S_{\text{cross-plane}}$ is relatively higher than $S_{\text{in-plane}}$ in the entire measurement range. The cumulative indicator of electrical charge transport, that is, PF ($=S^2\sigma$) is shown in Figure 5c. The PF increases with increasing temperature up to 450 K and decreases thereafter to reach a maximum $PF_{\text{in-plane}}$ of $\approx 4 \times 10^{-3}$ W m^{-1} K^{-2} and $PF_{\text{cross-plane}} \approx 3 \times 10^{-3}$ W m^{-1} K^{-2}. A higher PF was observed along the in-plane direction mainly because of higher $\sigma_{\text{in-plane}} \gg \sigma_{\text{cross-plane}}$.

The electronic thermal conductivity, κ_e, as shown in Figure 5d, can be experimentally evaluated according to the Wiedemann−Franz law $\kappa_e = L \times \sigma \times T$, where L is the Seebeck-dependent Lorenz number.[51] The L values shown in Supporting Information Figure S3 are estimated to be in the range of $(1.85-1.70) \times 10^{-8}$ W Ω K^{-2}. Like theoretical estimates, the experimental κ_e varies marginally in the measured temperature range and is higher along the in-plane direction, which is mainly due to higher $\sigma_{\text{in-plane}} \gg \sigma_{\text{cross-plane}}$. The evolution of specific heat capacity (C_p) with temperature is shown in Supporting Information Figure S4. The temperature-dependent C_p measurement of the synthesized nanostructured BST sample is higher and in closer proximity to the Dulong−Petit limit. Due to the disk-shaped sample requirement, the thermal diffusivity measurement was conducted only along the cross-plane direction for two sets of specimens prepared under similar sintering conditions.

The total thermal conductivity, κ, along the cross-plane (Figure 5e), was calculated using the equation $\kappa = D \times \rho \times C_p$. A drastic reduction in κ is observed mainly due to the nanoscale microstructural features (Figure 4) resulting from Te nanodomains and Sb precipitates within the BST−Te eutectic microstructure, which specifically targets the scattering of low-frequency phonons with a long mean free path. The lattice thermal conductivity, κ_L, is calculated using the equation $\kappa_L = \kappa - \kappa_e$ and is presented along with κ in Figure 5e. As seen from Figure 5d,e, both κ_L and κ_e had substantial contribution to the κ. While κ_e is mostly a direct outcome of σ and cannot be reduced further, a significant reduction in κ_L was observed. Although quantitatively identifying different contributions of the nanostructures (such as Te nanodomains and Sb precipitates) to the transport properties is complicated, their presence tends to scatter all phonons with mean free paths in all scales, ranging from the micron scale down to the atomic scale, thus drastically reducing the thermal conductivity.

3.4. BST Exhibiting a ZT_{max} of ≈ 1.4 at around 500 K.

Notably, both electrical and thermal transport measurements along the cross-plane direction for the thermally stabilized sample are analyzed for the estimation of ZT, to marginalize the effect of nonhomogeneity and crystallographic orientations introduced during sintering, thereby minimizing the possibility of erroneous data. The temperature-dependent ZT for the p-type BST nanocomposite prepared by colloidal synthesis

https://doi.org/10.1021/acs.jpcc.1c05375
J. Phys. Chem. C 2021, 125, 20184−20194

followed by SPS sintering is shown in Figure 5f. A maximum ZT_{max} of ≈ 1.4 at 500 K was attained due to the dramatically reduced κ with an enhanced PF. The synthesized BST nanocomposite displays suppressed bipolar conduction and enhanced phonon scattering at the interfaces. The characteristically low κ_L attained in BST was mainly attributed to the enhanced scattering of phonons by arrays of dislocations at semicoherent grain boundaries, nanodomains, and distortions in the lattice structure (Figure 4). Such a eutectic microstructure selectively scatters phonons, while remaining as an ineffective scatterer for electrons/holes which have relatively longer wavelength, thus retaining a higher n, σ, and PF. A drastic reduction in κ_L with a synergistic enhancement in PF cumulatively results in a higher ZT.

From the application perspective in the case of high-temperature sources, it is recognized that Bi_2Te_3-based materials can be segmented at low-temperature ends, as they are the best-available TE materials at lower temperatures.[8] The concept of segmentation for increasing the TE efficiency requires that the difference in the TE compatibility factor, CF, for the two TE materials should be less than a factor of 2. The CF was estimated using $CF = \frac{\sqrt{1+ZT}-1}{\alpha T}$[52] and is shown alongside values of ZT in Figure 5f. The CF is comparable to that of the other state-of-the-art p-type available in mid-temperature regimes.[53−56] Thus, prepared p-type nanocomposites will be a suitable TE material for segmentation with high-temperature and mid-temperature TE materials for achieving highly efficient TE-based power generation.

4. DISCUSSION

4.1. Comparison of Theoretical Calculations and Experimental Measurements. Despite the availability of a wide range of studies on the BST system, the comparison of transport characteristics between the bulk crystalline material and nanostructured samples requires complex considerations. The hole concentration of p-type $(Bi,Sb)_2Te_3$ alloys can be altered by adjusting the Bi−Sb ratio or by preparation of materials in different thermodynamic states (*e.g.*, Bi−Sb-rich or Te-rich conditions). This is primarily due to the occurrence of substantial doping in Bi_2Te_3-based materials *via* lattice defects, which alters the free carrier density and therefore the transport properties in a wider range.[47,57−59] The relatively smaller difference in electronegativity and atomic sizes of Sb−Te in comparison with those of Bi−Te in the synthesized BST induces antisite defects, whose concentrations depend majorly upon the stoichiometric composition, temperature, and processing conditions under which the material was synthesized.

In the nanostructured material, a higher concentration of defects exists especially at NP interfaces.[60−62] Therefore, it is more insightful to compare experimental measurements with the theoretically calculated properties, estimated at the value of chemical potential, yielding the same free carrier concentration as measured experimentally. For this purpose, we compared the measured TE properties with the theoretical predictions from the Boltzmann transport theory and density functional theory-calculated band structure for the $BiSbTe_3$ crystal. To acknowledge the effect of additional doping from defects and phase interfaces, the value of chemical potential for the calculation of transport coefficients was chosen to reproduce the experimentally measured charge carrier density. It is evident from Figure 5 that the experimental cross-plane and in-plane electrical transports are best described by the components of the TE coefficients along the hexagonal unit cell (c-axis) and perpendicular to it (along the ab plane), respectively. It was interesting to observe that while the measured σ and κ_e agree well with theoretical predictions, the measured thermopower (Seebeck coefficient) was substantially higher than theoretical estimates. This is an interesting observation, as it displays that the prepared nanocomposite sustains bulk-like electric conductivity, while suppressing lattice thermal conduction. The noticeable deviation of thermopower can be interpreted to be an effect of additional interfaces between semiconducting and metallic phases.[63]

The synthesized bulk nanocomposite exhibits a eutectic-type microstructure and Te-rich nanodomains and Sb-rich nanoprecipitates. After sintering, the Te-rich nanorods were found to exist as Te-rich eutectic phases, which are very effective for enhancing phonon scattering, as observed previously.[30,33,40,64] To understand the implication of microstructural features for enhancing phonon scattering in the synthesized BST nanocomposites, a Debye−Callaway model-based simulation was employed for calculating the lattice thermal conductivity by the following expression[65]

$$\kappa_L = \frac{k_B}{2\pi^2 v}\left(\frac{k_B T}{\hbar}\right)^3 \int_0^{\theta_D/T} \tau(x)\frac{x^4 e^x}{(e^x-1)^2}\,dx = \int_0^{\theta_D/T} \kappa_s(x)\,dx \quad (1)$$

where x is defined as $\hbar\omega/k_BT$ and $\hbar$, ω, v, and θ_D represent the reduced Planck constant, phonon frequency, average phonon velocity, and Debye temperature, respectively. Depending upon the material processing, various phonon scattering mechanisms occur within a material, which synergistically contribute toward phonon scattering. These phonon scattering mechanisms exhibit different frequency dependencies and therefore scatter different wavelengths of phonons, and hence, it is reasonable to integrate them using Matthiessen's rule as

$$\tau^{-1} = \tau_{bulk}^{-1} + \tau_{grain}^{-1} + \tau_{precipitates}^{-1} \quad (2)$$

For the bulk materials, the impurity (τ_{PD}^{-1}) and anharmonic ($\tau_U^{-1} + \tau_N^{-1}$) contributions in their standard forms are integrated as ($\tau_{bulk}^{-1} = \tau_U^{-1} + \tau_N^{-1} + \tau_{PD}^{-1}$). However, in the synthesized BST nanocomposites, two additional terms, representing the contributions to phonon scattering from the nanostructuring (τ_{grain}^{-1}) and from the precipitates ($\tau_{precipitates}^{-1}$), have been taken into consideration, to cover the wide phonon frequency range from atomic defects to microscale structures. The effect of Te-rich nanodomains and Sb-rich nanoprecipitates is threefold: they act as localized scattering centers, induce dense dislocations, and change the effective medium for phonons, which also affect the anharmonicity associated with τ_{bulk}^{-1}. For comparison, the lattice thermal conductivity was estimated using the Debye−Callaway method (ignoring the contribution of bipolar diffusion) for $Bi_{0.5}Sb_{1.5}Te_3$, $(Bi,Sb)Te_3$ bulk alloys, and the synthesized BST nanocomposite, which is shown in Figure 6a alongside experimentally measured κ_L of the synthesized BST nanocomposite and $Bi_{0.5}Sb_{1.5}Te_3$ + excess Te reported previously.[18]

Taking into consideration the scattering from Umklapp, normal, and point defects only, $(Bi,Sb)Te_3$ alloys exhibit stronger reduction of κ_L than the $Bi_{0.5}Sb_{1.5}Te_3$ alloy, which is

https://doi.org/10.1021/acs.jpcc.1c05375
J. Phys. Chem. C 2021, 125, 20184−20194

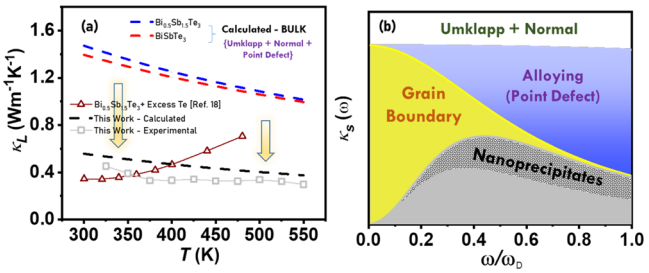

Figure 6. (a) Temperature-dependent lattice thermal conductivity (κ_L) calculated for $Bi_{0.5}Sb_{1.5}Te_3$, $(Bi,Sb)Te_3$ alloys, and the BST nanocomposite using the Debye−Callaway model (ignoring the contribution of bipolar diffusion) along with experimentally measured κ_L for comparison with $Bi_{0.5}Sb_{1.5}Te_3$ + excess Te.[18] (b) Frequency-dependent spectral thermal conductivity $\kappa_s(\omega)$ of the synthesized BST nanocomposite, indicating the contribution of different phonon scattering mechanisms.

mainly attributed to extra alloy disorder scattering. Remarkably, when grain boundary scattering is taken into consideration along with scattering from nanoprecipitates, a drastic reduction in κ_L is predicted, which is in line with previous observations for bulk nanostructured Te-rich $(Bi,Sb)Te_3$ alloys.[18,30,33,40,64] As shown in Figure 6a, in comparison to $Bi_{0.5}Sb_{1.5}Te_3$ + excess Te reported previously,[18] wherein only a Te-rich phase was observed, the as-synthesized BST nanocomposite exhibits a greater reduction in κ_L with an absence of bipolar conduction. The Te nanodomains and Sb nanoprecipitates (Figure 4) result in further lowering of κ_L owing to the combined effect on phonon scattering from nanoprecipitates and dislocations. To evaluate the contribution of different scattering processes, spectral thermal conductivity at room temperature is estimated using the Debye−Callaway model. As indicated in Figure 6b, an additional contribution is provided by Te nanodomains and Sb nanoprecipitates, to lower the κ_L in a wider frequency range, while suppressing the commonly occurring bipolar conduction in $(Bi,Sb)Te_3$ alloys.

4.2. Correlation of Phase Constitutions with High TE Performance. In the $(Bi,Sb)Te_3$ alloy system, the processing temperature and the nominal composition are key factors which determine both the formation of phases and the composition of these phases.[46,47] The preparation of the bulk nanostructured $(Bi,Sb)Te_3$ alloy is often challenging, as indicated by the Bi−Sb−Te phase diagram, which reveals structurally similar competing phases, such as $BiSbTe_3$, Sb_2Te_3, BiTe, and Bi_3Te_4, with close formation energies.[47,66] Moreover, propensity toward nonstoichiometry and tellurium volatility often induces atomic disorder such as antisite defects (Te_{Bi-Sb}; $Bi-Sb_{Te}$) and vacancies (Bi−Sb; Te).[34,46,47] Concurrently, formation of a Te-rich eutectic liquid phase was observed in excess Te compositions of $(Bi,Sb)Te_{3+x}$ alloys, particularly when Te spilling during sintering is controlled.[18,33,40,67]

In the synthesized BST nanocomposites, the presence of Te-rich precipitates and sintering near eutectic temperature was found to induce Sb nanoprecipitation, as observed previously in $(Bi,Sb)Te_3$ alloys.[30,39,40,45] This may be attributed to the high solubility of Bi and Sb in the Te liquid, which contributes to the rapid mass transport and rearrangement of the grains during liquid-phase sintering.[18] The solubility of Sb in the Te-rich liquid phase incurs atomic disorder and compositional variation within the $(Bi,Sb)Te_3$ matrix, which alters the Bi−Sb ratio within the $(Bi,Sb)Te_3$ matrix.[50] The atomic reordering of the Bi−Sb ratio, migration of the Sb- to Te-rich eutectic phase, and Sb vacancies in the $(Bi,Sb)Te_3$ matrix altogether resulted in intrinsic hole doping with large hole concentration, as evident by Hall effect measurements. Thus, remarkably high n results in higher σ and, correspondingly, a lower Seebeck coefficient at near room temperature, corresponding to stoichiometric $Bi_{0.5}Sb_{1.5}Te_3$ alloys.[8] The structural characterization of the as-synthesized nanopowder revealed the coexistence of three phases—specifically, structurally similar (layered structures with hexagonal symmetry and larger c-axis lattice constants) plate-like-shaped $(Bi,Sb)_2Te_3$ and Bi_4Te_3 compounds, together with one rod-like-shaped Te phase corresponding to the excess Te taken during colloidal synthesis. These NPs were then used as building blocks for bottom-up fabrication of the nanostructured bulk BST material employing SPS.

The uniaxial pressure and sintering near eutectic temperature of BST assist the favorable microstructural changes, forming Te-rich nanodomains and Sb-rich precipitation within the eutectic microstructure of the resultant BST nanocomposite. While the Te phase corresponding to Te-rich nanorods within the synthesized NPs promotes Sb_{Te} antisite defects, resulting in higher n, σ, and PF, the presence of Te nanodomains and Sb precipitates led to significant lowering in κ_L. A maximum ZT of ≈ 1.4 at 500 K of the BST nanocomposite prepared by novel colloidal synthesis followed by SPS consolidation is comparable to that of the state-of-the-art p-type BST-based alloys. In particular, Figure 7 shows a

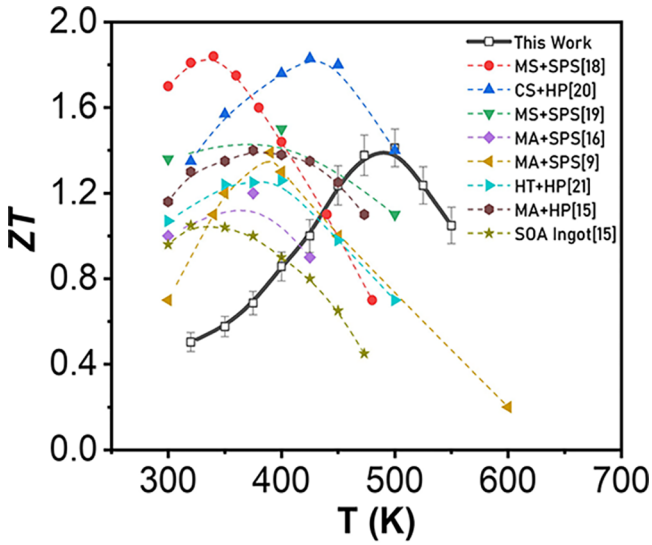

Figure 7. ZT comparison with state-of-the-art p-type $(Bi,Sb)_2Te_3$ nanostructured bulk alloys.

comparison of the synthesized BST nanocomposite with previously reported bulk nanostructured $(Bi,Sb)_2Te_3$ prepared by different methodologies, such as mechanical alloying,[9,15,16] melt spinning,[18,19] hydrothermal,[21] and chemical synthesis,[20] along with a state-of-the-art ingot.[15] High achieved ZT emphasizes the prospect of the reported material for waste heat recovery in low-temperature regime TE devices.

4.3. Low-Temperature TE-Based Power Generators by Suppressed Bipolar Conduction. Commercial TE technology at near room temperature has been predominantly led by Bi_2Te_3-based Peltier cooling materials. Harvesting the

https://doi.org/10.1021/acs.jpcc.1c05375
J. Phys. Chem. C 2021, 125, 20184−20194

low-grade waste heat available in low-temperature regimes is also an active area of research, particularly for rapidly growing markets of wearable electronics. In this context, TE-based power generators can be reliably employed for the recovery of low-temperature waste heat having low quality and low energy density. The TE performance of Bi_2Te_3, which is largely reported as a pseudo-binary phase of Bi_2Te_3 and Sb_2Te_3, is majorly impeded by minority carrier excitation across the small band gap even at room temperature; thus, a larger band gap is needed for higher temperature operation in which a high thermal gradient is available. The semiconducting band gap[68] using the temperature (T_{max}) at which the thermopower (S) peaks $E_g = 2e|S_{max}|T_{max}$, was roughly estimated to be ≈0.19 eV, which is a narrow band gap in between the bands of the binary compound Bi_2Te_3 (0.13 eV) and Sb_2Te_3 (0.28 eV).[49] The modification of the crystalline structure and electronic density of states in the synthesized bulk nanocomposite by Te-rich nanodomains and Sb precipitation is found to be effective in inhibiting the onset of intrinsic conduction for suppressed bipolar diffusion. The average ZT_{avg} of ≈ 1.1 was observed in the range of 300−500 K, indicating a wider prospect of the synthesized BST nanocomposite for application in low-temperature TE power generation.

5. CONCLUSIONS

A facile and scalable colloidal synthesis successfully afforded a mixed-phase nanopowder with plate- and rod-like morphologies of the constituent NPs. The as-synthesized nanopowder was subsequently consolidated at rapid heating rates employing SPS. The resultant bulk BST nanocomposite demonstrates an average ZT value of 1.1 in the 300−550 K temperature regime. The observed TE performance is associated with high n and reduced κ_L due to the BST−Te eutectic microstructure exhibiting Te nanodomains and Sb precipitates. A maximum ZT of ≈ 1.4 was attained at 500 K, which is among the highest reported values at a higher temperature for p-type bulk nanostructured BST materials (Figure 7). The attained higher ZT resembles the ones processed by top-down approaches (such as ball milling[9,15,16] and melt spinning[18,19]) and therefore exhibits considerable promise for fabricating commercial TE devices at low cost by thermochemical synthesis followed by SPS.

DATA AVAILABILITY STATEMENT

The data that support the findings of this study are available upon request from the authors.

ASSOCIATED CONTENT

Supporting Information

The Supporting Information is available free of charge at https://pubs.acs.org/doi/10.1021/acs.jpcc.1c05375.

Additional details of structural characterization; TE transport; *ab initio* calculations; and lattice thermal conductivity simulation *via* the Debye−Callaway model (PDF)

AUTHOR INFORMATION

Corresponding Authors

Nagendra S. Chauhan − *International Iberian Nanotechnology Laboratory (INL), Braga 4715-330, Portugal; Plasmonics and Perovskites Laboratory, Indian Institute of Technology, Kanpur, Kanpur, Uttar Pradesh 208016, India;* orcid.org/0000-0003-2579-6642; Email: nagendra599@gmail.com

Yury V. Kolen'ko − *International Iberian Nanotechnology Laboratory (INL), Braga 4715-330, Portugal;* orcid.org/0000-0001-7493-1762; Phone: +351 253 140 112 (ext. 2534); Email: yury.kolenko@inl.int; Fax: (351) 253 140 119

Authors

Sergey V. Pyrlin − *Centro de Física das Universidades do Minho e do Porto, Universidade do Minho, Braga 4710-057, Portugal;* orcid.org/0000-0001-5180-2175

Oleg I. Lebedev − *Laboratoire CRISMAT, UMR 6508, CNRS-Ensicaen, Caen 14050, France*

Luis S. A. Marques − *Centro de Física das Universidades do Minho e do Porto, Universidade do Minho, Braga 4710-057, Portugal*

Marta M. D. Ramos − *Centro de Física das Universidades do Minho e do Porto, Universidade do Minho, Braga 4710-057, Portugal*

Tanmoy Maiti − *Plasmonics and Perovskites Laboratory, Indian Institute of Technology, Kanpur, Kanpur, Uttar Pradesh 208016, India;* orcid.org/0000-0003-1581-7614

Kirill Kovnir − *Department of Chemistry, Iowa State University, Ames, Iowa 50011, United States; Ames Laboratory, United States Department of Energy, Ames, Iowa 50011, United States;* orcid.org/0000-0003-1152-1912

Brian A. Korgel − *McKetta Department of Chemical Engineering and Texas Materials Institute, The University of Texas at Austin, Austin, Texas 78712, United States;* orcid.org/0000-0001-6242-7526

Complete contact information is available at: https://pubs.acs.org/10.1021/acs.jpcc.1c05375

Notes

The authors declare no competing financial interest.

ACKNOWLEDGMENTS

We thank the members of the Nanochemistry Research Group (http://nanochemgroup.org) at INL for insightful discussions and support. This work was supported by the Portuguese national funding agency for science, research, and technology (FCT) under the UT-BORN-PT project (UTAP-EXPL/CTE/0050/2017), strategic project UID/FIS/04650/2020, Project SATRAP (POCI-01-0145-FEDER-028108) and Advanced Computing Project CPCA /A2/4513/2020 for access to MACC-BOB HPC resources. B.A.K. acknowledges funding of this work by the Robert A. Welch Foundation (grant no. F-1464). N.S.C. and T.M. acknowledge SERB, India (project no. SPO/SERB/MET/2018547) for financial support.

REFERENCES

(1) Bell, L. E. Cooling, heating, generating power, and recovering waste heat with thermoelectric systems. *Science* **2008**, *321*, 1457−1461.

(2) Tarancón, A. Powering the IoT revolution with heat. *Nat. Electron.* **2019**, *2*, 270−271.

(3) Haras, M.; Skotnicki, T. Thermoelectricity for IoT−A review. *Nano Energy* **2018**, *54*, 461−476.

(4) Petsagkourakis, I.; Tybrandt, K.; Crispin, X.; Ohkubo, I.; Satoh, N.; Mori, T. Thermoelectric materials and applications for energy harvesting power generation. *Sci. Technol. Adv. Mater.* **2018**, *19*, 836−862.

(5) Snyder, G. J.; Toberer, E. S. Complex thermoelectric materials. *Nat. Mater.* **2008**, *7*, 105−114.
(6) DiSalvo, F. J. Thermoelectric cooling and power generation. *Science* **1999**, *285*, 703−706.
(7) Jouhara, H.; Khordehgah, N.; Almahmoud, S.; Delpech, B.; Chauhan, A.; Tassou, S. A. Waste heat recovery technologies and applications. *Therm. Sci. Eng. Prog.* **2018**, *6*, 268−289.
(8) Goldsmid, H. Bismuth telluride and its alloys as materials for thermoelectric generation. *Materials* **2014**, *7*, 2577−2592.
(9) Li, H.; Jing, H.; Han, Y.; Xu, Y.; Lu, G.-Q.; Xu, L. Microstructure and transport properties of copper-doped p-type BiSbTe alloy prepared by mechanical alloying and subsequent spark plasma sintering. *J. Alloys Compd.* **2013**, *576*, 369−374.
(10) Cui, J. L.; Xue, H. F.; Xiu, W. J.; Yang, W.; Xu, X. B. Thermoelectric properties of Cu-doped p-type pseudo-binary $Cu_xBi_{0.5}Sb_{1.5-x}Te_3$ (x= 0.05−0.4) alloys prepared by spark plasma sintering. *Scr. Mater.* **2006**, *55*, 371−374.
(11) Huang, H.; Li, J.; Chen, S.; Zhang, Z.; Yan, Y.; Su, X.; Tang, X. Anisotropic thermoelectric transport properties of $Bi_{0.5}Sb_{1.5}Te_{2.96+x}$ zone melted ingots. *J. Solid State Chem.* **2020**, *288*, 121433.
(12) Lee, J. K.; Park, S. D.; Kim, B. S.; Oh, M. W.; Cho, S. H.; Min, B. K.; Lee, H. W.; Kim, M. H. Control of thermoelectric properties through the addition of Ag in the $Bi_{0.5}Sb_{1.5}Te_3$ alloy. *Electron. Mater. Lett.* **2010**, *6*, 201−207.
(13) Cui, J. L.; Xu, X. B. Transport properties of quaternary Ag−Bi−Sb−Te alloys prepared by pressureless sintering. *Mater. Lett.* **2005**, *59*, 3205−3208.
(14) Kim, K.; Kim, G.; Lee, H.; Lee, K. H.; Lee, W. Band engineering and tuning thermoelectric transport properties of p-type $Bi_{0.52}Sb_{1.48}Te_3$ by Pb doping for low-temperature power generation. *Scr. Mater.* **2018**, *145*, 41−44.
(15) Poudel, B.; Hao, Q.; Ma, Y.; Lan, Y.; Minnich, A.; Yu, B.; Yan, X.; Wang, D.; Muto, A.; Vashaee, D.; Chen, X.; Liu, J.; Dresselhaus, M. S.; Chen, G.; Ren, Z. High-thermoelectric performance of nanostructured bismuth antimony telluride bulk alloys. *Science* **2008**, *320*, 634−638.
(16) Bulat, L. P.; Drabkin, I. A.; Karatayev, V. V.; Osvenskii, V. B.; Parkhomenko, Y. N.; Lavrentev, M. G.; Sorokin, A. I.; Pshenai-Severin, D. A.; Blank, V. D.; Pivovarov, G. I.; Bublik, V. T.; Tabachkova, N. Y. Structure and transport properties of bulk nanothermoelectrics based on $Bi_xSb_{2-x}Te_3$ fabricated by SPS method. *J. Electron. Mater.* **2013**, *42*, 2110−2113.
(17) Pan, Y.; Aydemir, U.; Grovogui, J. A.; Witting, I. T.; Hanus, R.; Xu, Y.; Wu, J.; Wu, C. F.; Sun, F. H.; Zhuang, H. L.; Dong, J. F.; Li, J. F.; Dravid, V. P.; Snyder, G. J. Melt-Centrifuged $(Bi, Sb)_2Te_3$: Engineering Microstructure toward High Thermoelectric Efficiency. *Adv. Mater.* **2018**, *30*, 1802016.
(18) Kim, S. I.; Lee, K. H.; Mun, H. A.; Kim, H. S.; Hwang, S. W.; Roh, J. W.; Yang, D. J.; Shin, W. H.; Li, X. S.; Lee, Y. H.; Snyder, G. J.; Kim, S. W. Dense dislocation arrays embedded in grain boundaries for high-performance bulk thermoelectrics. *Science* **2015**, *348*, 109−114.
(19) Xie, W.; Wang, S.; Zhu, S.; He, J.; Tang, X.; Zhang, Q.; Tritt, T. M. High performance Bi_2Te_3 nanocomposites prepared by single-element-melt-spinning spark-plasma sintering. *J. Mater. Sci.* **2013**, *48*, 2745−2760.
(20) Liu, Y.; Zhang, Y.; Ortega, S.; Ibáñez, M.; Lim, K. H.; Grau-Carbonell, A.; Martí-Sánchez, S.; Ng, K. M.; Arbiol, J.; Kovalenko, M. V.; Cadavid, D.; Cabot, A. Crystallographically Textured Nanomaterials Produced from the Liquid Phase Sintering of $Bi_xSb_{2-x}Te_3$ Nanocrystal Building Blocks. *Nano Lett.* **2018**, *18*, 2557−2563.
(21) Chen, Z.; lin, M. Y.; Xu, G. D.; Chen, S.; Zhang, J. H.; Wang, M. M. Hydrothermal synthesized nanostructure Bi−Sb−Te thermoelectric materials. *J. Alloys Compd.* **2014**, *588*, 384−387.
(22) Misra, D. K.; Sumithra, S.; Chauhan, N. S.; Nolting, W. M.; Poudeu, P. F. P.; Stokes, K. L. Correlation between microstructure and drastically reduced lattice thermal conductivity in bismuth telluride/bismuth nanocomposites for high thermoelectric figure of merit. *Mater. Sci. Semicond. Process.* **2015**, *40*, 453−462.
(23) Pakdel, A.; Guo, Q.; Nicolosi, V.; Mori, T. Enhanced thermoelectric performance of Bi−Sb−Te/Sb_2O_3 nanocomposites by energy filtering effect. *J. Mater. Chem. A* **2018**, *6*, 21341−21349.
(24) Li, J.; Tan, Q.; Li, J.-F.; Liu, D.-W.; Li, F.; Li, Z.-Y.; Zou, M.; Wang, K. BiSbTe-based nanocomposites with high ZT: the effect of SiC nanodispersion on thermoelectric properties. *Adv. Funct. Mater.* **2013**, *23*, 4317−4323.
(25) Madavali, B.; Lee, C.-H.; Kim, H.-S.; Lee, K.-H.; Hong, S.-J. Investigation of microstructure and thermoelectric properties of p-type BiSbTe/ZnO composites. *Int. J. Appl. Ceram. Technol.* **2018**, *15*, 125−131.
(26) Li, Y.; Dou, Y.; Qin, X.; Zhang, J.; Xin, H.; Li, D.; Song, C.; Zou, T.; Liu, Y.; Li, C. Enhanced thermoelectric figure of merit in p-type β-Zn_4Sb_3/$Bi_{0.4}Sb_{1.6}Te_3$ nanocomposites. *RSC Adv.* **2016**, *6*, 12243−12248.
(27) Jiang, Z.; Ming, H.; Qin, X.; Feng, D.; Zhang, J.; Song, C.; Li, D.; Xin, H.; Li, J.; He, J. Achieving High Thermoelectric Performance in p-Type BST/PbSe Nanocomposites through the Scattering Engineering Strategy. *ACS Appl. Mater. Interfaces* **2020**, *12*, 46181−46189.
(28) Madavali, B.; Kim, H.-S.; Lee, K.-H.; Hong, S.-J. Enhanced Seebeck coefficient by energy filtering in Bi-Sb-Te based composites with dispersed Y_2O_3 nanoparticles. *Intermetallics* **2017**, *82*, 68−75.
(29) Dou, Y. C.; Qin, X. Y.; Li, D.; Li, L. L.; Zou, T. H.; Wang, Q. Q. Enhanced thermopower and thermoelectric performance through energy filtering of carriers in $(Bi_2Te_3)_{0.2}(Sb_2Te_3)_{0.8}$ bulk alloy embedded with amorphous SiO_2 nanoparticles. *J. Appl. Phys.* **2013**, *114*, 044906.
(30) Zhuang, H. L.; Pei, J.; Cai, B.; Dong, J.; Hu, H.; Sun, F. H.; Pan, Y.; Snyder, G. J.; Li, J. F. Thermoelectric performance enhancement in BiSbTe alloy by microstructure modulation via cyclic spark plasma sintering with liquid phase. *Adv. Funct. Mater.* **2021**, *31*, 2009681.
(31) Jo, S.; Park, S. H.; Ban, H. W.; Gu, D. H.; Kim, B.-S.; Son, J. H.; Hong, H.-K.; Lee, Z.; Han, H.-S.; Jo, W.; Lee, J. E.; Son, J. S. Simultaneous improvement in electrical and thermal properties of interface-engineered BiSbTe nanostructured thermoelectric materials. *J. Alloys Compd.* **2016**, *689*, 899−907.
(32) Deng, R.; Su, X.; Zheng, Z.; Liu, W.; Yan, Y.; Zhang, Q.; Dravid, V. P.; Uher, C.; Kanatzidis, M. G.; Tang, X. Thermal conductivity in $Bi_{0.5}Sb_{1.5}Te_{3+x}$ and the role of dense dislocation arrays at grain boundaries. *Sci. Adv.* **2018**, *4*, No. eaar5606.
(33) Qin, H.; Zhang, Y.; Cai, S.; Sun, Y.; Wang, W.; Xie, L.; Sun, S.; Qin, D.; Guo, M.; Guo, F.; Wu, H.; Zhang, Q.; Cai, W.; Sui, J. Critical Role of Tellurium Self-Compensation in Enhancing the Thermoelectric Performance of p-Type $Bi_{0.4}Sb_{1.6}Te_3$ Alloy. *Chem. Eng. J.* **2021**, *425*, 130670.
(34) Hu, L.; Zhu, T.; Liu, X.; Zhao, X. Point defect engineering of high-performance bismuth-telluride-based thermoelectric materials. *Adv. Funct. Mater.* **2014**, *24*, 5211−5218.
(35) Zhu, T.; Hu, L.; Zhao, X.; He, J. New insights into intrinsic point defects in V_2VI_3 thermoelectric materials. *Adv. Sci.* **2016**, *3*, 1600004.
(36) Soni, A.; Shen, Y.; Yin, M.; Zhao, Y.; Yu, L.; Hu, X.; Dong, Z.; Khor, K. A.; Dresselhaus, M. S.; Xiong, Q. Interface driven energy filtering of thermoelectric power in spark plasma sintered $Bi_2Te_{2.7}Se_{0.3}$ nanoplatelet composites. *Nano Lett.* **2012**, *12*, 4305−4310.
(37) Nethravathi, C.; Rajamathi, C. R.; Rajamathi, M.; Maki, R.; Mori, T.; Golberg, D.; Bando, Y. Synthesis and thermoelectric behaviour of copper telluride nanosheets. *J. Mater. Chem. A* **2014**, *2*, 985−990.
(38) Fu, J.; Song, S.; Zhang, X.; Cao, F.; Zhou, L.; Li, X.; Zhang, H. Bi_2Te_3 nanoplates and nanoflowers: Synthesized by hydrothermal process and their enhanced thermoelectric properties. *CrystEngComm* **2012**, *14*, 2159−2165.
(39) Pan, Y.; Qiu, Y.; Witting, I.; Zhang, L.; Fu, C.; Li, J.-W.; Huang, Y.; Sun, F.-H.; He, J.; Snyder, G. J.; Felser, C.; Li, J.-F. Synergistic modulation of mobility and thermal conductivity in $(Bi, Sb)_2Te_3$ towards high thermoelectric performance. *Energy Environ. Sci.* **2019**, *12*, 624−630.

https://doi.org/10.1021/acs.jpcc.1c05375
J. Phys. Chem. C 2021, 125, 20184−20194

(40) Cai, B.; Zhuang, H.-L.; Pei, J.; Su, B.; Li, J.-W.; Hu, H.; Jiang, Y.; Li, J.-F. Spark plasma sintered Bi-Sb-Te alloys derived from ingot scrap: Maximizing thermoelectric performance by tailoring their composition and optimizing sintering time. *Nano Energy* **2021**, *85*, 106040.
(41) Chauhan, N. S.; Lebedev, O. I.; Kovnir, K.; Pyrlin, S. V.; Marques, L. S. A.; Ramos, M. M. D.; Korgel, B. A.; Kolen'ko, Y. V. Scalable colloidal synthesis of $Bi_2Te_{2.7}Se_{0.3}$ plate-like particles give access to a high-performing n-type thermoelectric material for low temperature application. *Nanoscale Adv.* **2020**, *2*, 5699−5709.
(42) Sousa, V.; Gonçalves, B. F.; Franco, M.; Ziouani, Y.; González-Ballesteros, N.; Fátima Cerqueira, M.; Yannello, V.; Kovnir, K.; Lebedev, O. I.; Kolen'ko, Y. V. Superstructural Ordering in Hexagonal $CuInSe_2$ Nanoparticles. *Chem. Mater.* **2018**, *31*, 260−267.
(43) Gonçalves, B. F.; LaGrow, A. P.; Pyrlin, S.; Owens-Baird, B.; Botelho, G.; Marques, L. S. A.; Ramos, M. M. D.; Kovnir, K.; Lanceros-Mendez, S.; Kolen'ko, Y. V. Large-Scale Synthesis of Semiconducting Cu (In, Ga)Se_2 Nanoparticles for Screen Printing Application. *Nanomaterials* **2021**, *11*, 1148.
(44) Rodríguez-Carvajal, J. Recent advances in magnetic structure determination by neutron powder diffraction. *Phys. B* **1993**, *192*, 55−69.
(45) Chen, Y.-H.; Liao, C.-N. Transport properties of electrically sintered bismuth antimony telluride with antimony nanoprecipitation. *Appl. Phys. Lett.* **2017**, *111*, 143901.
(46) Hyun, D.-B.; Oh, T. S.; Hwang, J.-S.; Shim, J.-D. J. S. m. Effect of excess Te addition on the thermoelectric properties of the 20% Bi_2Te_3-80% Sb_2Te_3 single crystal and hot-pressed alloy. *Scr. Mater.* **2001**, *44*, 455−460.
(47) Witting, I. T.; Chasapis, T. C.; Ricci, F.; Peters, M.; Heinz, N. A.; Hautier, G.; Snyder, G. J. The thermoelectric properties of bismuth telluride. *Adv. Electron. Mater.* **2019**, *5*, 1800904.
(48) Shi, E.; Cui, S.; Kempf, N.; Xing, Q.; Chasapis, T.; Zhu, H.; Li, Z.; Bahk, J.-H.; Snyder, G. J.; Zhang, Y. J. N. R. Origin of inhomogeneity in spark plasma sintered bismuth antimony telluride thermoelectric nanocomposites. *Nano Res.* **2020**, *13*, 1339−1346.
(49) Hu, L.-P.; Zhu, T.-J.; Wang, Y.-G.; Xie, H.-H.; Xu, Z.-J.; Zhao, X.-B. Shifting up the optimum figure of merit of p-type bismuth telluride-based thermoelectric materials for power generation by suppressing intrinsic conduction. *NPG Asia Mater.* **2014**, *6*, No. e88.
(50) Lan, Y.; Poudel, B.; Ma, Y.; Wang, D.; Dresselhaus, M. S.; Chen, G.; Ren, Z. Structure study of bulk nanograined thermoelectric bismuth antimony telluride. *Nano Lett.* **2009**, *9*, 1419−1422.
(51) Kim, H.-S.; Gibbs, Z. M.; Tang, Y.; Wang, H.; Snyder, G. J. Characterization of Lorenz number with Seebeck coefficient measurement. *APL Mater.* **2015**, *3*, 041506.
(52) Snyder, G. J.; Ursell, T. S. Thermoelectric efficiency and compatibility. *Phys. Rev. Lett.* **2003**, *91*, 148301.
(53) Bhardwaj, A.; Chauhan, N. S.; Misra, D. K. Significantly enhanced thermoelectric figure of merit of p-type Mg_3Sb_2-based Zintl phase compounds via nanostructuring and employing high energy mechanical milling coupled with spark plasma sintering. *J. Mater. Chem. A* **2015**, *3*, 10777−10786.
(54) Chauhan, N. S.; Bhardwaj, A.; Senguttuvan, T. D.; Pant, R. P.; Mallik, R. C.; Misra, D. K. A synergistic combination of atomic scale structural engineering and panoscopic approach in p-type ZrCoSb-based half-Heusler thermoelectric materials for achieving high ZT. *J. Mater. Chem. C* **2016**, *4*, 5766−5778.
(55) Chauhan, N. S.; Bathula, S.; Vishwakarma, A.; Bhardwaj, R.; Johari, K. K.; Gahtori, B.; Dhar, A. Enhanced thermoelectric performance in p-type ZrCoSb based half-Heusler alloys employing nanostructuring and compositional modulation. *J. Materiomics* **2019**, *5*, 94−102.
(56) Vishwakarma, A.; Chauhan, N. S.; Bhardwaj, R.; Johari, K. K.; Dhakate, S. R.; Gahtori, B.; Bathula, S. Melt-Spun SiGe Nano-Alloys: Microstructural Engineering Towards High Thermoelectric Efficiency. *J. Electron. Mater.* **2021**, *50*, 364−374.
(57) Lošťák, P.; Drašar, Č.; Bachan, D.; Beneš, L.; Krejčová, A. Defects in $Bi_2Te_{3-x}Se_x$ single crystals. *Radiat. Eff. Defects Solids* **2010**, *165*, 211−215.
(58) Horák, J.; Navrátil, J.; Starý, Z.; Solids, C. o. Lattice point defects and free-carrier concentration in $Bi_{2+x}Te_3$ and $Bi_{2+x}Se_3$ crystals. *J. Phys. Chem. Solids* **1992**, *53*, 1067−1072.
(59) Liu, W.-S.; Zhang, Q.; Lan, Y.; Chen, S.; Yan, X.; Zhang, Q.; Wang, H.; Wang, D.; Chen, G.; Ren, Z. Thermoelectric property studies on Cu-doped n-type $Cu_xBi_2Te_{2.7}Se_{0.3}$ nanocomposites. *Adv. Energy Mater.* **2011**, *1*, 577−587.
(60) Zhang, Q.; Fang, T.; Liu, F.; Li, A.; Wu, Y.; Zhu, T.; Zhao, X. Tuning Optimum Temperature Range of Bi_2Te_3-Based Thermoelectric Materials by Defect Engineering. *Chem.—Asian J.* **2020**, *15*, 2775−2792.
(61) Duan, X.; Jiang, Y. Annealing effects on the structural and electrical transport properties of n-type $Bi_2Te_{2.7}Se_{0.3}$ thin films deposited by flash evaporation. *Appl. Surf. Sci.* **2010**, *256*, 7365−7370.
(62) Kim, S. J.; Choi, H.; Kim, Y.; We, J. H.; Shin, J. S.; Lee, H. E.; Oh, M.-W.; Lee, K. J.; Cho, B. J. Post ionized defect engineering of the screen-printed $Bi_2Te_{2.7}Se_{0.3}$ thick film for high performance flexible thermoelectric generator. *Nano Energy* **2017**, *31*, 258−263.
(63) Wang, Q.; Yang, L.; Zhou, S.; Ye, X.; Wang, Z.; Zhu, W.; McCluskey, M. D.; Gu, Y. Phase-defined Van der Waals Schottky junctions with significantly enhanced thermoelectric properties. *J. Phys. Chem. Lett.* **2017**, *8*, 2887−2894.
(64) Witting, I. T.; Grovogui, J. A.; Dravid, V. P.; Snyder, G. J. Thermoelectric transport enhancement of Te-rich bismuth antimony telluride ($Bi_{0.5}Sb_{1.5}Te_{3+x}$) through controlled porosity. *J. Materiomics* **2020**, *6*, 532−544.
(65) Callaway, J.; von Baeyer, H. C. Effect of point imperfections on lattice thermal conductivity. *Phys. Rev.* **1960**, *120*, 1149.
(66) Scherrer, H.; Martin-Lopez, R.; Lenoir, B.; Dauscher, A.; Scherrer, S. Thermoelectric materials of p and n type from the (Bi, Sb, Te) phase diagram. In *Proceedings ICT2001. 20 International Conference on Thermoelectrics (Cat. No. 01TH8589)*; IEEE, 2001; pp 13−17.
(67) Ha, H. P.; Cho, Y. W.; Byun, J. Y.; Shim, J. D. The effect of excess tellurium on the thermo electric properties of Bi_2Te_3-Sb_2Te_3 solid solutions. *J. Phys. Chem. Solids* **1994**, *55*, 1233−1238.
(68) Gibbs, Z. M.; Kim, H.-S.; Wang, H.; Snyder, G. J. Band gap estimation from temperature dependent Seebeck measurement—deviations from the $2e|S|_{max}T_{max}$ relation. *Appl. Phys. Lett.* **2015**, *106*, 022112.

https://doi.org/10.1021/acs.jpcc.1c05375
J. Phys. Chem. C 2021, 125, 20184−20194